JOURNAL OF SPACECRAFT AND ROCKETS
Vol. 42, No. 2, March–April 2005

Numerical Study of Turbulent Flows over Launch Vehicle Configurations

Enda Dimitri V. Bigarella*
Instituto Tecnológico de Aeronáutica, 12228-900 São José dos Campos, Brazil
and
João Luiz F. Azevedo†
Centro Técnico Aeroespacial, 12228-904 São José dos Campos, Brazil

Turbulent flow simulations aimed at improving the capability of representing launch-vehicle aerodynamics are presented. A three-dimensional finite difference numerical code, written for general, curvilinear, body-conforming coordinate systems, is used. Simulations of turbulent flows over a flat plate are compared to theoretical and empirical results in order to assess the correctness of the implementation of the formulation. Transonic and supersonic turbulent flows are then simulated over the Brazilian satellite launch-vehicle configuration. Two eddy viscosity turbulence models are chosen for this numerical method, considering single- and two-equation closures. These two closures, namely, the Spalart–Allmaras single-equation model and Menter's shear-stress-transport two-equation model, have been natively developed for aerospace applications. In general, good results within engineering error margins are obtained with the method presented here.

Nomenclature

a	=	speed of sound
Cp	=	pressure coefficient
d	=	artificial dissipation term
$\bar{\boldsymbol{E}}, \bar{\boldsymbol{F}}, \bar{\boldsymbol{G}}$	=	inviscid flux vectors
$\bar{\boldsymbol{E}}_v, \bar{\boldsymbol{F}}_v, \bar{\boldsymbol{G}}_v$	=	viscous flux vectors
e	=	total energy per unit volume
e_i	=	internal energy
f	=	source term of the multigrid method
J	=	Jacobian of the coordinate transformation
k	=	turbulent kinetic energy
Pr	=	Prandtl number
p	=	static pressure
$\bar{\boldsymbol{Q}}$	=	vector of conserved properties
$\boldsymbol{q}$	=	heat-flux vector
Re	=	Reynolds number
RHS	=	right-hand-side operator
S	=	strain-rate tensor
$\mathcal{S}$	=	constant of the Sutherland law
T	=	static temperature
U, V, W	=	contravariant velocity components
u, v, w	=	Cartesian velocity components
x, y, z	=	Cartesian coordinates
α	=	angle of attack
$\alpha_1 \ldots \alpha_5$	=	Runge–Kutta control parameters
γ	=	ratio of specific heats
Δt	=	time step
μ	=	dynamic viscosity coefficient
ν	=	kinematic viscosity coefficient
$\tilde{\nu}$	=	modified eddy viscosity coefficient
ξ, η, ζ	=	general curvilinear coordinates
ρ	=	density
τ	=	viscous stress tensor
Ω	=	rotation tensor
ω	=	turbulent dissipation

Subscripts

i, j, k	=	grid node coordinates
ℓ	=	laminar property
m	=	current grid of the multigrid method
t	=	turbulent property
∞	=	freestream property

Superscripts

n	=	time instant
$*$	=	dimensional property

Presented as Paper 2003-0602 at the AIAA 41st Aerospace Sciences Meeting, Reno, NV, 6–9 January 2003; received 5 December 2003; revision received 22 March 2004; accepted for publication 29 March 2004.

*Ph.D. Student, Department of Aerodynamics, Division of Aeronautical Engineering, CTA/ITA/IEAA; enda_bigarella@yahoo.it.

†Senior Research Engineer, Space System Division, Instituto de Aeronáutica e Espaço, CTA/IAE/ASE-N; azevedo@iae.cta.br. Senior Member AIAA.

Introduction

LAUNCH vehicles are typically designed to fly at very low angles of attack. Nevertheless, even at such flight conditions the lateral loads that arise in these vehicles are quite large, and they must be accurately determined. Therefore, during the design process, one is required to determine the aerodynamics of these vehicles at angle of attack because this provides the loads required for the structural design of the vehicle as well as the flight dynamics stability characteristics necessary for the control system design. Previous work[1–3] at Instituto de Aeronáutica e Espaço (IAE) has presented axisymmetric viscous simulations for flows over the Brazilian satellite launch vehicle (VLS) with very good representation of the aerodynamics. Moreover, three-dimensional inviscid computations over the VLS at low angles of attack with good agreement with experimental data were also performed.[4] This earlier work, however, considered fairly simple three-dimensional geometries, and mesh refinement was less than adequate because of computational resource limitations.

Further development in the computational resources in the country in the 1990s made possible the simulation of more realistic flows, and, thus, axisymmetric turbulent flows and three-dimensional laminar viscous flow simulations could be performed with adequate mesh refinement. Furthermore, axisymmetric meshes could be made refined enough to capture the dependency of the formulation with the Reynolds number.[5] The results presented in that work showed the influence of the turbulence modeling in the flow topology. Reference 6 has shown three-dimensional results over general-launch-vehicle configurations. The calculations emphasized that a laminar viscous formulation could not correctly capture some of the flow phenomena that might occur in the simulations of interest at IAE.

Obviously, this is what one should expect because the Reynolds numbers of interest are of the order of 10^7. Clearly, phenomena such as flow separation caused by adverse pressure gradients and shock-wave boundary-layer interactions are poorly represented by a laminar formulation at such high Reynolds numbers. Nevertheless, these phenomena play an important role in the flows over launch vehicles, and, therefore, they should be adequately simulated.

The present work is aimed at addressing the implementation and validation of turbulent closures for a finite difference computational tool under development at IAE.[7] Hence, numerical results for the subsonic turbulent flow over a flat plate are compared to known data in the literature in order to assess the correctness of the turbulent formulation added to the code. Furthermore, the computational code is used to simulate three-dimensional transonic and supersonic flows about the VLS. This vehicle is a four-stage satellite launcher built with four boosters attached to the main body. Because experimental data are available for this configuration, the numerical results are compared to them such that the code effectiveness in the solution of realistic aerospace configuration flows can be assessed. More details on the experimental results for the VLS configuration, obtained through extensive wind-tunnel tests, can be found in Ref. 8. In the present work, computations were performed considering only the vehicle central body. The solver used is a three-dimensional finite difference code written for general, body-conforming, curvilinear coordinate systems, and it solves the compressible Reynolds-averaged Navier–Stokes equations.

Theoretical Formulation

The numerical code solves the dimensionless three dimensional, compressible Reynolds-averaged Navier–Stokes (RANS) equations. These equations can be written in strong conservation-law form for general, body-conforming, curvilinear coordinates[9] as

$$\frac{\partial \bar{\boldsymbol{Q}}}{\partial \tau}+\frac{\partial \bar{\boldsymbol{E}}}{\partial \xi}+\frac{\partial \bar{\boldsymbol{F}}}{\partial \eta}+\frac{\partial \bar{\boldsymbol{G}}}{\partial \zeta}=\frac{\partial \bar{\boldsymbol{E}}_v}{\partial \xi}+\frac{\partial \bar{\boldsymbol{F}}_v}{\partial \eta}+\frac{\partial \bar{\boldsymbol{G}}_v}{\partial \zeta} \tag{1}$$

where the vector of conserved quantities $\bar{\boldsymbol{Q}}$ is defined as

$$\bar{\boldsymbol{Q}}=J^{-1}[\rho \quad \rho u \quad \rho v \quad \rho w \quad e]^T \tag{2}$$

The inviscid flux vectors $\bar{\boldsymbol{E}}$, $\bar{\boldsymbol{F}}$, and $\bar{\boldsymbol{G}}$ and the viscous flux vectors $\bar{\boldsymbol{E}}_v$, $\bar{\boldsymbol{F}}_v$, and $\bar{\boldsymbol{G}}_v$ can be written as

$$A=J^{-1}\begin{Bmatrix}\rho C\\ \rho u C+p\psi_x\\ \rho v C+p\psi_y\\ \rho w C+p\psi_z\\ (e+p)C-p\psi_t\end{Bmatrix} \tag{3}$$

$$A_v=\frac{J^{-1}}{Re}\begin{Bmatrix}0\\ \psi_x\tau_{xx}+\psi_y\tau_{xy}+\psi_z\tau_{xz}\\ \psi_x\tau_{xy}+\psi_y\tau_{yy}+\psi_z\tau_{yz}\\ \psi_x\tau_{xz}+\psi_y\tau_{yz}+\psi_z\tau_{zz}\\ \psi_x\beta_x+\psi_y\beta_y+\psi_z\beta_z\end{Bmatrix} \tag{4}$$

where $A=\bar{\boldsymbol{E}},\bar{\boldsymbol{F}}$, or $\bar{\boldsymbol{G}}$; $A_v=\bar{\boldsymbol{E}}_v,\bar{\boldsymbol{F}}_v$, or $\bar{\boldsymbol{G}}_v$; $\psi=\xi,\eta$, or ζ; and $C=U$, V, or W, respectively. The contravariant velocity components U, V, and W are defined as

$$\begin{aligned}U&=\xi_t+\xi_x u+\xi_y v+\xi_z w\\ V&=\eta_t+\eta_x u+\eta_y v+\eta_z w\\ W&=\zeta_t+\zeta_x u+\zeta_y v+\zeta_z w\end{aligned} \tag{5}$$

Throughout this work, the curvilinear coordinate system is defined such that ξ is the rocket longitudinal direction, positive downstream, η is the wall-normal direction, and ζ is the circumferential direction. Expressions for the Jacobian of the transformation J and for the various metric terms can be found in Ref. 9. All of the equations were implemented in dimensionless form, and the reference conditions used in this work are also identical to those indicated in Ref. 9.

The stress tensor terms in Eq. (4) are given as

$$\tau_{ij}=(\mu_\ell+\mu_t)\left[\left(\frac{\partial u_i}{\partial x_j}+\frac{\partial u_j}{\partial x_i}\right)-\frac{2}{3}\frac{\partial u_m}{\partial x_m}\delta_{ij}\right] \tag{6}$$

where

$$x_i=(x,y,z), \qquad u_i=(u,v,w) \tag{7}$$

represent the Cartesian coordinates and the Cartesian velocity components, respectively. The heat-flux vector components are defined as

$$q_j=-\gamma\left(\frac{\mu_\ell}{Pr}+\frac{\mu_t}{Pr_t}\right)\frac{\partial e_i}{\partial x_j} \tag{8}$$

where e_i is defined as a function of the dimensionless temperature as

$$e_i=T/\gamma(\gamma-1) \tag{9}$$

The equation of state is given in its dimensionless form as

$$p=(\gamma-1)\left[e-\tfrac{1}{2}\rho(u^2+v^2+w^2)\right] \tag{10}$$

Variables β_x, β_y, and β_z are defined as

$$\beta_i=\tau_{ij}u_j-q_i \tag{11}$$

The variation of the dynamic viscosity coefficient with the temperature is given by the Sutherland equation as

$$\mu_\ell=T^{\frac{3}{2}}[(1+\mathcal{S})/(T+\mathcal{S})] \tag{12}$$

where $\mathcal{S}=110/T^*_\infty$ and T^*_∞ is the dimensional reference temperature in degrees Kelvin.

The Reynolds number, based on the freestream speed of sound a_∞, density ρ_∞, viscosity $\mu_{\ell\infty}$, and vehicle diameter D, is given as $Re=\rho_\infty a_\infty D/\mu_{\ell\infty}$. As one can observe in the formulation presented earlier, the Boussinesq hypothesis is used in this work in order to include the turbulent effects in the formulation. Thus, the dynamic viscosity coefficient μ can be written as $\mu=\mu_\ell+\mu_t$, where μ_ℓ is the laminar viscosity coefficient and μ_t is the eddy viscosity coefficient, obtained through the chosen turbulence models.

Numerical Implementation

The governing equations are discretized in a finite difference context. The adopted spatial discretization uses a central difference algorithm plus explicitly added artificial dissipation terms. Such terms are included in the formulation in order to control nonlinear instabilities. The equations, fully discretized in space, can be written as

$$\left(\frac{\partial \bar{Q}}{\partial \tau}\right)_{i,j,k}=-\mathrm{RHS}_{i,j,k} \tag{13}$$

The right-hand-side (RHS) operator of Eq. (13) is defined as

$$\begin{aligned}\mathrm{RHS}_{i,j,k}=&\frac{\bar{E}_{i+1,j,k}-\bar{E}_{i-1,j,k}}{2\Delta\xi}-\frac{\bar{E}_{v_{i+\frac{1}{2},j,k}}-\bar{E}_{v_{i-\frac{1}{2},j,k}}}{\Delta\xi}\\ &+\frac{\bar{F}_{i,j+1,k}-\bar{F}_{i,j-1,k}}{2\,\Delta\eta}-\frac{\bar{F}_{v_{i,j+\frac{1}{2},k}}-\bar{F}_{v_{i,j-\frac{1}{2},k}}}{\Delta\eta}\\ &+\frac{\bar{G}_{i,j,k+1}-\bar{G}_{i,j,k-1}}{2\Delta\zeta}-\frac{\bar{G}_{v_{i,j,k+\frac{1}{2}}}-\bar{G}_{v_{i,j,k-\frac{1}{2}}}}{\Delta\zeta}\\ &-\frac{J^{-1}_{i+\frac{1}{2},j,k}\,d_{i+\frac{1}{2},j,k}-J^{-1}_{i-\frac{1}{2},j,k}\,d_{i-\frac{1}{2},j,k}}{\Delta\xi}\end{aligned}$$

$$-\frac{J^{-1}_{i,j+\frac{1}{2},k}\, d_{i,j+\frac{1}{2},k} - J^{-1}_{i,j-\frac{1}{2},k}\, d_{i,j-\frac{1}{2},k}}{\Delta\eta}$$

$$-\frac{J^{-1}_{i,j,k+\frac{1}{2}}\, d_{i,j,k+\frac{1}{2}} - J^{-1}_{i,j,k-\frac{1}{2}}\, d_{i,j,k-\frac{1}{2}}}{\Delta\zeta} \tag{14}$$

where $\Delta\xi = \Delta\eta = \Delta\zeta = 1$ for the general curvilinear coordinate case. The artificial dissipation is represented by the d terms in Eq. (14). An anisotropic, scalar artificial dissipation method, as described in Ref. 10, is used. This scheme is nonlinear and allows a selection between artificial dissipation terms of second and fourth differences, which is very important for capturing shock waves in the flow.

The time-marching procedure uses an explicit, second-order, five-stage Runge–Kutta scheme, derived from the ideas presented in Ref. 11, which can be written as

$$\bar{Q}^{(0)}_{i,j,k} = \bar{Q}^{n}_{i,j,k}$$

$$\bar{Q}^{(\ell)}_{i,j,k} = \bar{Q}^{(0)}_{i,j,k} - \alpha_\ell \Delta t_{i,j,k}\, \mathrm{RHS}^{(\ell-1)}_{i,j,k}, \qquad \bar{Q}^{n+1}_{i,j,k} = \bar{Q}^{(5)}_{i,j,k} \tag{15}$$

where $\ell = 1, 2, \ldots, 5$. Numerical values for the α_ℓ parameters can be found in Ref. 12. In the preceding expressions, Δt stands for the time step, and n and $n+1$ refer to the property values at the start and at the end of each time step.

Convergence Acceleration Techniques

Equation (15) indicates that a local time-step option is being used in order to accelerate convergence to steady-state calculations. This is done by means of the Courant–Friedrichs–Lewy (CFL) number definition. Furthermore, an implicit residual smoothing technique, as described in Ref. 13, is used to allow the use of larger CFL numbers. Furthermore, a multigrid algorithm of the full-approximation-storage type is also considered. This method is based on exchanging both solution and residue values between different grid levels.[14,15] For the problem being solved, written in an operatorlike form, $Lq = f$, the algorithm works as follows:

1) Presmoothing: execute n_1 iterations of the time-marching procedure at level $L_0\, q_0 = f_0$.

2) For grids $m = 0$ to $M-1$,

a) Residue computing:

$$r_m = f_m - L_m q_m$$

b) Residue restriction:

$$r_{m+1} = R(r_m)$$

c) Solution restriction:

$$q'_{m+1} = R(q_m)$$

d) RHS computation in the next coarser mesh:

$$f_{m+1} = r_{m+1} + L_{m+1} q'_{m+1}$$

e) Presmoothing: execute n_1 iterations of the time-marching procedure in level $m+1$, $L_{m+1} q_{m+1} = f_{m+1}$.

3) Solve the problem for the coarsest grid, $L_M q_M = f_M$, executing n_M iterations.

4) For grids $m = M$ to 1,

a) Solution correction:

$$q_{m-1} = q_{m-1} - P(q_m - q'_m)$$

b) Postsmoothing: execute n_2 iterations of the time-marching procedure in level $m-1$, $L_{m-1} q_{m-1} = f_{m-1}$.

In this algorithm, r represents the RHS operator, at time instant n, augmented by a multigrid source term f, which represents the residue information exchange between adjacent grid levels. Moreover, q represents the conserved variables at the same time instant n. The subscript m denotes the operation for the mth grid level. The number of grid levels of this process is $M+1$, where M is associated with the coarsest grid level and 0 with the finest one. Operator R represents the restriction of conserved properties and residues from a grid level to the next coarser level, which is done by a nine-point interpolation operator. Operator P interpolates from a grid level to the next finer one by a trilinear interpolation.

The description made before starts with an approximation to the solution on the finest grid. A V or a W cycle is used to reach the coarsest grid and back again to the finest one in order to improve the solution. This is an appropriate strategy if a good approximation of the solution in this finest mesh is available. This is not normally the case in the present work because the simulations start with the freestream flow as the initial solution. For high-speed flows, such as the ones usually simulated here, this can also represent a problem for the iteration method because extremely high gradients are present in the solution at the first initial iterations. To improve the multigrid algorithm as well as the computational method, the simulations start at the coarsest grid level. Some iterations with the Runge–Kutta time stepping are performed at this grid, and a high-order interpolation is performed to the next finer grid. Some multigrid cycles are, then, performed to improve the solution at this grid. This procedure is repeated successively until the finest grid is reached, with a good initial guess to the solution. Multigrid cycles are, then, performed on the finest mesh, using the algorithm previously defined, until convergence is reached. This technique is usually denoted as a full-multigrid method. Furthermore, viscous terms are computed on every grid level, and a cheaper second-difference artificial dissipation model can be used on the coarser grids to save computational resources.

Turbulence Models

As already discussed, turbulence models based on the Boussinesq hypothesis are chosen for this numerical code. Previous work[5] has shown, in axisymmetric simulations, that advanced turbulence closures are required to correctly address the flow phenomena that can occur about the geometries of interest for the group. Thus, a single- and a two-equation turbulence model, which have originally been designed for aerospace applications, are chosen for this work. The turbulence equations of both models are solved in a loosely coupled fashion with the Navier–Stokes system. An alternating-direction-implicit (ADI) method, similar to a Beam and Warming scheme,[16] is chosen for the time stepping of the turbulence equations. Artificial viscosity is added to control nonlinear instabilities through an upwind discretization of the advective terms of the turbulence equations. This approach is used for both right- and left-hand-side operators of the system. The upwind discretization chosen is a flux-vector splitting-type approach similar to the Steger and Warming method.[17]

Spalart–Allmaras (SA) Model

The chosen single-equation model is the one proposed in Ref. 18. This model, rewritten for compressible flow and considering a general, body-conforming coordinate system, is given in its dimensionless form as

$$\frac{\partial \bar{\tilde{\mu}}}{\partial \tau} + \frac{\partial(\bar{\tilde{\mu}} U_j)}{\partial \xi_j} = J^{-1} \rho c_{b1} \tilde{S} \tilde{\nu} + \frac{J^{-1}}{\sigma Re}\left\{ \frac{\partial}{\partial x_j}\left[(\mu_\ell + \tilde{\mu}) \frac{\partial \tilde{\nu}}{\partial x_j} \right] + c_{b2} \frac{\partial \tilde{\nu}}{\partial x_k} \frac{\partial \tilde{\nu}}{\partial x_k} \right\} - J^{-1} \frac{1}{Re} \rho c_{w1} f_w \left(\frac{\tilde{\nu}}{d} \right)^2 \tag{16}$$

where x_j has already been defined in Eq. (7), $\xi_i = (\xi, \eta, \zeta)$ are the curvilinear coordinate system coordinates, and $U_i = (U, V, W)$ are the contravariant velocity components.

The variable solved for by this equation $\bar{\tilde{\mu}}$ is defined as $\bar{\tilde{\mu}} = J^{-1}\tilde{\mu}$, where $\tilde{\mu} = \rho\tilde{\nu}$. Variable $\tilde{\nu}$ relates to the eddy viscosity by

$$\nu_t = \tilde{\nu} f_{v1}, \qquad f_{v1} = \chi^3 \Big/ \left(\chi^3 + {c_{v1}}^3\right), \qquad \chi = \tilde{\nu}/\nu_\ell \tag{17}$$

where ν_ℓ is the laminar kinematic viscosity coefficient.

The production term $\tilde{S}$ is given by

$$\tilde{S} = S + (1/Re)(\tilde{\nu}/\kappa^2 d^2) f_{v2}, \qquad f_{v2} = 1 - \chi/(1 + \chi f_{v1}) \tag{18}$$

where S is the magnitude of the vorticity vector

$$S = \sqrt{2\Omega_{ij}\Omega_{ij}}, \qquad \Omega_{ij} = \frac{1}{2}\left(\frac{\partial u_i}{\partial x_j} - \frac{\partial u_j}{\partial x_i}\right) \tag{19}$$

and u_i has already been defined in Eq. (7). Variable d represents the distance to the closest wall. The wall damping function f_w is

$$f_w = g\left[\frac{1 + {c_{w3}}^6}{g^6 + {c_{w3}}^6}\right]^{\frac{1}{6}}, \qquad g = r + c_{w2}(r^6 - r)$$

$$r = \frac{1}{Re}\frac{\tilde{\nu}}{\tilde{S}\kappa^2 d^2} \tag{20}$$

Boundary conditions are $\tilde{\nu} = 0$ at the wall and $\tilde{\nu} = 0.1\nu_{\ell\infty}$ at freestream boundaries. A zeroth-order extrapolation is chosen for other boundaries. Initial conditions are the same as the freestream values. The model constants are $c_{b1} = 0.1355$, $\sigma = \frac{2}{3}, c_{b2} = 0.622, \kappa = 0.41, c_{w1} = c_{b1}/\kappa + (1 + c_{b2})/\sigma, c_{w2} = 0.3$, $c_{w3} = 2$, and $c_{v1} = 7.1$.

Baseline/Shear-Stress-Transport Model

The chosen two-equation closure is the shear-stress-transport model (SST) proposed in Ref. 19. This model is derived from both the famous $k-\omega$ (Ref. 20) and the standard $k-\epsilon$ (Ref. 21) models. It solves some reported problems of the $k-\omega$ closure regarding freestream value dependency[22] while keeping the better numerical behavior of this model at the wall, when compared to $k-\epsilon$ closures. The SST model, rewritten for compressible flow and considering a general, body-conforming coordinate system, can be given in its dimensionless form as

$$\frac{\partial \bar{k}}{\partial \tau} + \frac{\partial(\bar{k}U_j)}{\partial \xi_j} = \frac{J^{-1}}{Re}P_k - J^{-1}\beta^*\rho\omega k + \frac{J^{-1}}{Re}\frac{\partial}{\partial x_j}\left[(\mu_\ell + \mu_t\sigma_k)\frac{\partial k}{\partial x_j}\right] \tag{21}$$

$$\frac{\partial \bar{\omega}}{\partial \tau} + \frac{\partial(\bar{\omega}U_j)}{\partial \xi_j} = J^{-1}\frac{\gamma_t}{\nu_t}P_k - J^{-1}\beta_1\rho\omega^2 + \frac{J^{-1}}{Re}\frac{\partial}{\partial x_j}\left[(\mu_\ell + \mu_t\sigma_\omega)\frac{\partial \omega}{\partial x_j}\right] + J^{-1}2(1 - F_1)\rho\sigma_{\omega 2}\frac{1}{\omega}\frac{\partial k}{\partial x_j}\frac{\partial \omega}{\partial x_j} \tag{22}$$

The turbulent variables solved for by this set of transport equations are given by

$$\bar{k} = J^{-1}\rho k, \qquad \bar{\omega} = J^{-1}\rho\omega \tag{23}$$

The production term is given by

$$P_k = \mu_t\left[\left(\frac{\partial u_i}{\partial x_j} + \frac{\partial u_j}{\partial x_i}\right)\frac{\partial u_i}{\partial x_j} - \frac{2}{3}\left(\frac{\partial u_m}{\partial x_m}\right)^2\right] - \frac{2}{3}Re\rho k\frac{\partial u_n}{\partial x_n} \tag{24}$$

Model constants are generally calculated as

$$\phi = F_1\phi_1 + (1 - F_1)\phi_2 \tag{25}$$

where ϕ_1 represents the set of constants for the $k-\omega$ model and ϕ_2 the set for the standard $k-\epsilon$ model. The following sets for ϕ in the preceding equation are used:

$$\sigma_{k1} = 0.5, \qquad \sigma_{\omega 1} = 0.5, \qquad \beta_1 = 0.075$$

$$\gamma_{t1} = \beta_1 \big/ \beta^* - \sigma_{\omega 1}\kappa^2 \big/ \sqrt{\beta^*} \tag{26}$$

$$\sigma_{k2} = 1.0, \qquad \sigma_{\omega 2} = 0.855, \qquad \beta_2 = 0.0828$$

$$\gamma_{t2} = \beta_2 \big/ \beta^* - \sigma_{\omega 2}\kappa^2 \big/ \sqrt{\beta^*} \tag{27}$$

$$\beta^* = 0.09, \qquad \kappa = 0.41 \tag{28}$$

The F_1 variable is a blending function that turns on the k–ω closure near walls and the standard $k-\epsilon$ outside boundary layers. It is given by

$$F_1 = \tanh\left(arg_1^4\right) \tag{29}$$

$$arg_1 = \min\left[\max\left(\frac{\sqrt{k}}{0.09\omega d}, \frac{500\nu_\ell}{Re\omega d^2}\right), \frac{4\rho\sigma_{\omega 2}k}{CD_{k\omega}d^2}\right] \tag{30}$$

$$CD_{k\omega} = \max\left(2\rho\sigma_{\omega 2}\frac{1}{\omega}\frac{\partial k}{\partial x_j}\frac{\partial \omega}{\partial x_j}, 10^{-20}\right) \tag{31}$$

The eddy viscosity, for the SST model, is defined by

$$\nu_t = \frac{Rea_1 k}{\max(a_1\omega, F_2\Omega)} \tag{32}$$

inside boundary layers, where Ω is the absolute value of the vorticity. The F_2 variable is another blending function that turns this new definition on inside boundary layers. It is defined as

$$F_2 = \tanh\left(arg_2^2\right) \tag{33}$$

$$arg_2 = \max\left(2\frac{\sqrt{k}}{0.09\omega d}, \frac{500\nu_\ell}{Re\omega d^2}\right) \tag{34}$$

For the baseline model (BSL), a simpler version of the SST model, the eddy viscosity is defined as

$$\nu_t = Re(k/\omega) \tag{35}$$

Because a measure of the turbulent kinetic energy is used in this model, it should be included in the total energy and in the viscous terms of the RANS equations. Therefore, the static pressure is redefined as

$$p = (\gamma - 1)\left[e - \tfrac{1}{2}\rho(u^2 + v^2 + w^2) - \rho k\right] \tag{36}$$

and the internal energy, as

$$e_i = (e/\rho) - \tfrac{1}{2}(u^2 + v^2 + w^2) - k \tag{37}$$

The dimensionless components of the viscous stress tensor, given in Eq. (6), are rewritten, for a Newtonian fluid, as

$$\tau_{ij} = (\mu_\ell + \mu_t)\left[\left(\frac{\partial u_i}{\partial x_j} + \frac{\partial u_j}{\partial x_i}\right) - \frac{2}{3}\frac{\partial u_m}{\partial x_m}\delta_{ij}\right] - \frac{2}{3}Re\rho k\delta_{ij} \tag{38}$$

Furthermore, a gradient of the kinetic turbulent energy must be considered in the conservation of energy within the field. Hence, the components β_x, β_y, and β_z are rewritten as

$$\beta_i = \tau_{ij}u_j - q_i + r_i, \qquad r_i = (\mu_\ell + \sigma_{k1}\mu_t)\frac{\partial k}{\partial x_i} \tag{39}$$

The following set of freestream conditions is chosen:

$$\omega_\infty = 10(M_\infty/L), \qquad \nu_{t\infty} = 10^{-3}\nu_{\ell\infty}$$

$$k_\infty = (1/Re)\nu_{t\infty}\omega_\infty \tag{40}$$

where L is the approximate length of the computational domain. Wall boundary conditions considered are

$$k = 0, \qquad \omega = 60(1/Re)\left[\nu_\ell \Big/ \beta_1(\Delta y_1)^2\right] \tag{41}$$

where Δy_1 is the distance to the wall of the closest point away from it. Zeroth-order extrapolation is performed at other boundaries.

Boundary Conditions and Computational Grids

For the configurations of interest here, the types of boundary conditions that should be considered include upstream (entrance), solid-wall, far-field, symmetry, upstream centerline, and downstream (exit) conditions. For the wall, the velocity vector is set to zero, and a zero-order extrapolation of the pressure and the density is performed. The rocket upstream centerline is a singularity of the coordinate transformation, and, hence, an adequate treatment of this boundary must be provided. In the present case, the approach consists in extrapolating the property values from the adjacent longitudinal plane and in averaging the extrapolated values in the azimuthal direction in order to define the updated properties at the upstream centerline. At the exit and entrance planes, the boundary conditions are implemented through the use of the one-dimensional characteristic relations for the three-dimensional Euler equations. The interested reader is referred to Ref. 23 for further details on the use of one-dimensional characteristic relations for boundary condition implementation. Far-field boundaries are treated with the use of Riemann invariants[24] in order to avoid numerical difficulties.

To reduce computational costs, the grids used in the numerical simulations for the rocket configuration are generated for half a body in the azimuthal direction. This simplification is valid for the cases assessed in this work because low angles of attack are considered. This condition implies a symmetric flow about the pitching plane.[25] Hence, symmetry is applied in this pitching plane using two auxiliary planes. Those extra elements are added, respectively, before the leeside and after the windside pitching planes. In the case of the flat plate, spanwise symmetry boundary conditions are applied to the two extreme planes.

Furthermore, to correctly simulate the complicated turbulence dynamics that occur inside the boundary layers, a good mesh refinement in these regions is strongly recommended. In a straightforward practical way, the turbulent dimensionless parameter y^+ should be kept around one. This parameter is defined as $y^+ = y\sqrt{(Re/\nu_\ell)(\partial u/\partial y)}$, where y is the dimensionless distance to the wall of the first mesh point away from it. This condition is very important in turbulent simulations in order to preserve the balance between turbulent production and destruction inside the viscous sublayer. On the other hand, nevertheless, the robustness of the chosen turbulent models in the present effort allows the user to set this parameter at about three, which can save some important computational resources. The resulting grid for the VLS main body configuration, to which numerical results are mesh independent, has $161 \times 89 \times 21$ points. A view of a longitudinal plane of this grid is shown in Fig. 1. The final mesh for the flat plate configuration has $121 \times 90 \times 10$ points. A view of a longitudinal plane of this grid is also shown in Fig. 1. The flat-plate length comprises the last $\frac{3}{4}$ part of the total computational domain length. For the first $\frac{1}{4}$ section, symmetry boundary conditions are used.

Careful mesh-refinement studies of the present numerical method for the cases of interest in this paper are discussed in detail in Ref. 15. Various grid configurations for the VLS and the flat-plate cases have been simulated in order to achieve mesh-independent results. For the VLS case, meshes with $121 \times 50 \times 21$, $161 \times 89 \times 21$, and $201 \times 101 \times 21$ points have been used. Mesh independence was assessed through the comparison of pressure coefficient distributions. Similar study for the plate case has also been performed. In this case, the turbulent boundary-layer velocity distribution profile was the quantity used to assess mesh independence. Therefore, the statement that the computational simulations presented in this work are mesh independent is a result of the previously described mesh-refinement study. In Ref. 15, the numerical accuracy of the present computational code has been assessed using the method of manufactured solutions, as described in Ref. 26. The discussion in Ref. 15 also shows the low error levels that can be expected with the current implementation.

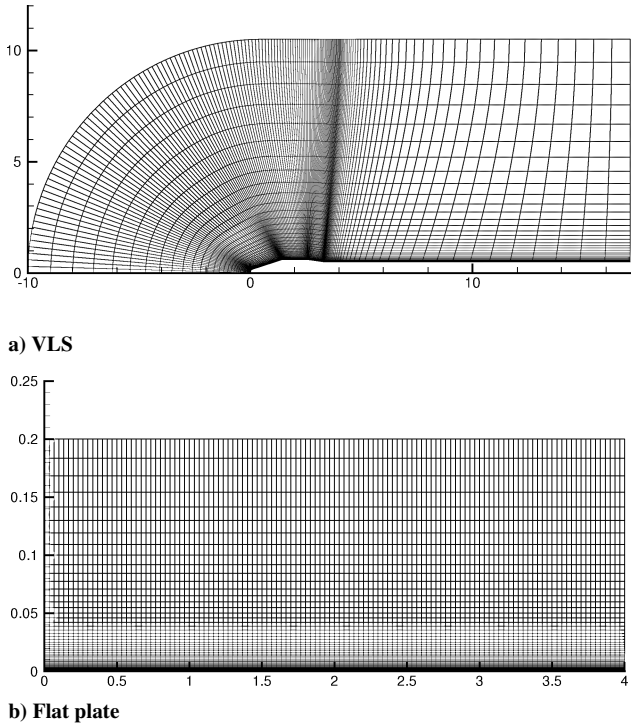

Fig. 1 Overall view of a plane from the computational grids used in the simulations performed.

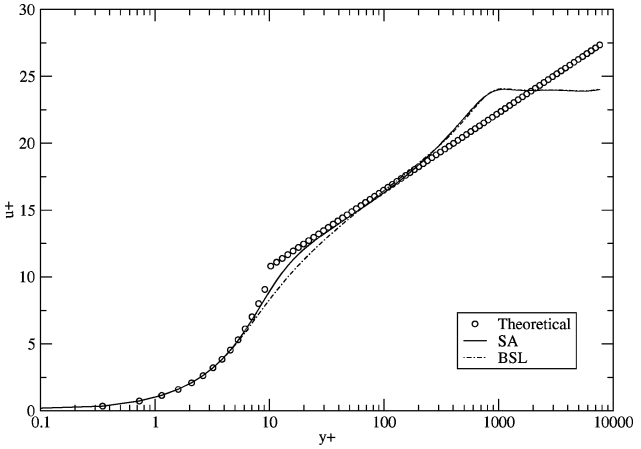

Fig. 2 Turbulent boundary layers for a zero-pressure-gradient flat plate. Reynolds number based on the plate length is $Re_c = 1 \times 10^6$.

Results and Discussion

In this section, the numerical results obtained with the formulation just presented are compared to known data in order to verify the correctness of the implementation and to assess the quality of the results that can be obtained with the current computational tool.

Flat-Plate Results

Figure 2 presents zero-pressure-gradient flat-plate turbulent boundary-layer profiles. One can observe in this figure the numerical curves obtained with the turbulence closures discussed before, namely, the single-equation SA and the two-equation BSL models. The theoretical log-layer profile is also shown in this figure in order to compare with the numerical results. The Reynolds number, based on the plate length, is $Re_c = 1 \times 10^6$. However, the results presented in Fig. 2 are independent of this parameter. It can be clearly seen in this figure that both numerical solutions compare very well with

the theoretical solution. This theoretical curve is given by small circles representing the mesh spacing along the normal direction to the wall. One can verify that the first grid point away from the wall has $y^+ \approx 0.4$, which is, by far, fine enough to correctly simulate a turbulent boundary layer with the closures discussed in this work. Small differences can be found between the two models in the intermediate sublayer region. The BSL model estimates a smoother velocity profile than that of the SA closure. However, both models estimate very well the viscous and inertial sublayers as well as the external layer. The results presented in Fig. 2 are indicative of the quality of the data that can be obtained with this numerical formulation.

VLS Results

In this section, numerical results for transonic and supersonic flows about the VLS second-stage flight configuration are presented. The numerical results are compared to available experimental data, obtained through numerous wind-tunnel tests,[8] in order to address the capability of the numerical method implemented. The inviscid and the laminar viscous formulation of the computational code presented here have already been extensively studied in previous work, as can be seen in Ref. 7. In that paper, a large range of flow conditions, such as transonic to supersonic speeds and various angles of attack, has been simulated. As a general assessment, good results within engineering error margins could be obtained, except for some flowfield regions where turbulence effects seemed to be important.

Transonic Flight Condition

A transonic flight condition, with freestream Mach number $M_\infty = 0.90$, angle of attack $\alpha = 0$ deg, and $Re = 25 \times 10^6$, is chosen because of its physical complexity. In this flight condition, a strong shock wave builds over the vehicle payload fairing, whereas other flow regions are still transonic, as will be seen in the forthcoming results. Besides the known mathematical complexity that this flow condition might impose on the simulation, this strong shock wave can interfere with the boundary layer in that region, interacting with it in a very complicated fashion. Previous axisymmetric results[5,27] showed that turbulence modeling is required to correctly capture the flow configuration in this region. As will be seen, the flow complexity is large enough to prevent the laminar formulation from converging to a steady-state solution.

Figure 3 presents experimental schlieren photograph and numerical density gradient contours over the VLS central body at freestream Mach number $M_\infty = 0.90$ and angle of attack $\alpha = 0$ deg. Various approximations to the Navier–Stokes equations are considered in this case, including an inviscid, a laminar viscous, and two turbulent approaches. For the latter computations, the SA and BSL models are chosen. A less refined mesh than presented in Fig. 1 has been used in the inviscid simulation. One can see in Fig. 3 that the inviscid and the turbulent results are qualitatively similar to the experimental data. The presence of a strong shock wave that builds over the vehicle payload fairing region is clear. One can also verify that the laminar result is much different from the experimental one. The laminar flow separates at the first expansion corner because of the weakness of the laminar boundary layer at such a high Reynolds number.

Figure 4 presents the numerical and experimental Cp wall distributions for the VLS at the described transonic flight condition. This figure shows numerical results obtained with the approximations discussed earlier. The oscillatory and nonsymmetrical behavior of the laminar result should be noted, which is indicative of the

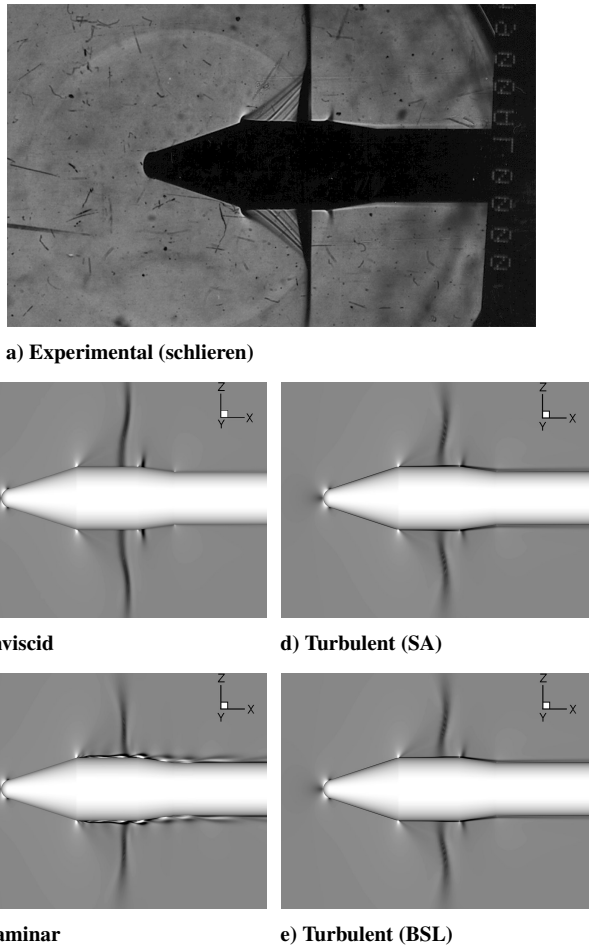

Fig. 3 Experimental schlieren photograph and numerical density gradient contours over the VLS second-stage configuration at $M_\infty = 0.90$, $\alpha = 0$ deg, and $Re = 25 \times 10^6$.

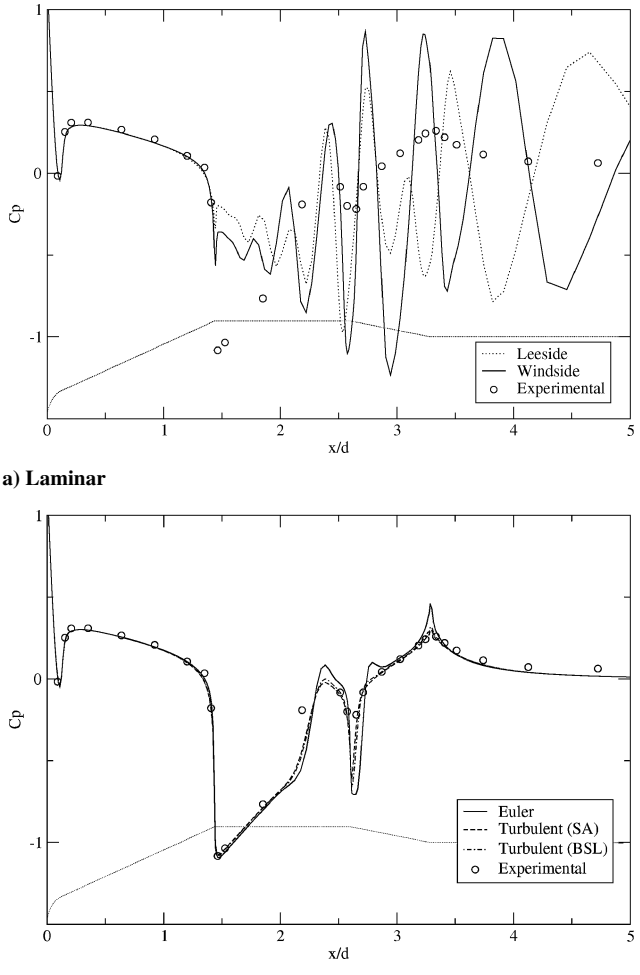

Fig. 4 Experimental and numerical Cp distributions over the VLS second-stage configuration at $M_\infty = 0.90$ and $\alpha = 0$ deg obtained with various formulations. $Re = 25 \times 10^6$.

transient characteristic of the numerical solution. Furthermore, it can be seen in Fig. 4 that the inviscid simulation presents overshoots at high gradient regions, such as the shock wave and sharp corners along the geometry. This behavior is well known for this formulation.[4,5] It can also be seen that the turbulent simulations have much better agreement with the experimental pressure distribution, if compared to the inviscid computations. Furthermore, both turbulence models perform in a very similar way in these simulations.

As already stated, the simulated computational model considers only the vehicle main body configuration. One should observe that, in the afterbody cylindrical section, all numerical results tend to return to the freestream pressure values, that is, $Cp = 0$. This is not true for the experimental data, which present small but nonzero Cp values in this region. This is clearly the influence of the VLS strap-on boosters, which are not included in the numerical simulations, but they are present in the wind-tunnel model. The aspects that concern the influence of the boosters can be addressed only with a multiblock capability in order to include the complete configuration in the computational model. Preliminary results with a laminar viscous formulation and a multiblock capability have already been obtained, as can be seen in Refs. 28 and 29.

Another important aspect that should be emphasized with regard to the turbulence modeling is the increase in the computational resources necessary to address the new equations added to the formulation. A simulation of a laminar flow costs 25% more than an inviscid one, whereas the same simulation with a single- and a two-equation turbulence model costs, respectively, 45 and 50% more than the laminar computations. Added to this is the fact that, as already stated, a turbulent simulation requires more refined and/or stretched grids in order to satisfy the $y^+ = 1$ condition for the first grid point away from the wall. The additional grid refinement increases the stiffness of the problem leading to lower convergence rates to the code, as one can observe in the residue histories presented in Fig. 5. In this figure the inviscid simulation, with a less refined and stretched grid, converges much faster then the turbulent cases. The separated flow, in the laminar simulation, has an unsteady behavior, and it keeps the computations from converging to a steady-state solution.

One can also observe in Fig. 5 residue histories for the turbulence-model equations. In the case of the SA model, the eddy viscosity variable $\tilde{\bar{\mu}}$ is plotted, whereas, for the SST model, the turbulent kinetic energy variable $\bar{k}$ is chosen. It can be seen in Fig. 5 that the turbulent equations converge when the governing equations converge to a steady-state solution. This is a good indication that, for typical CFL numbers that can be used with the explicit numerical method presented here, the ADI time-marching procedure of the turbulence equations, together with the upwind discretization of the advective terms of this system, is sufficient to control nonlinear instabilities arising in these equations. In other words, the turbulence equations do not spoil the convergence of the governing equations, which results in a more robust numerical tool for the applications of interest.

Mach-number contours for the VLS at angle of attack $\alpha = 4$ deg, $M_\infty = 0.90$, and $Re = 25 \times 10^6$ are presented in Fig. 6. The SST turbulence model has been used for such simulation. A further quantitative comparison of such simulation case can be found in Fig. 7. In this figure, numerical Cp distributions for the vehicle leeside- and windside are compared to the respective experimental results. One can clearly observe in this figure very good approximation between numerical and experimental results. The numerical code

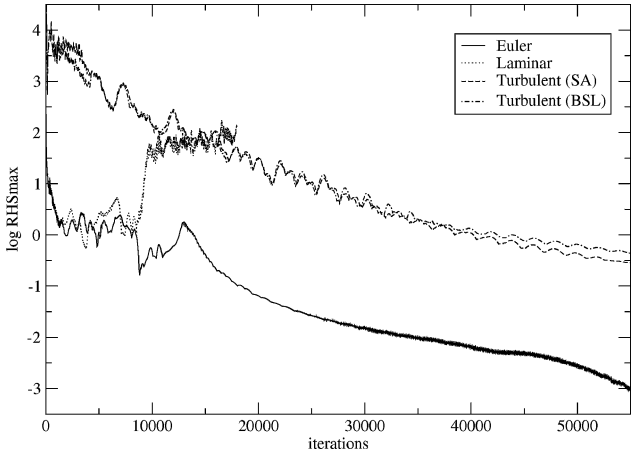

a) Continuity equation

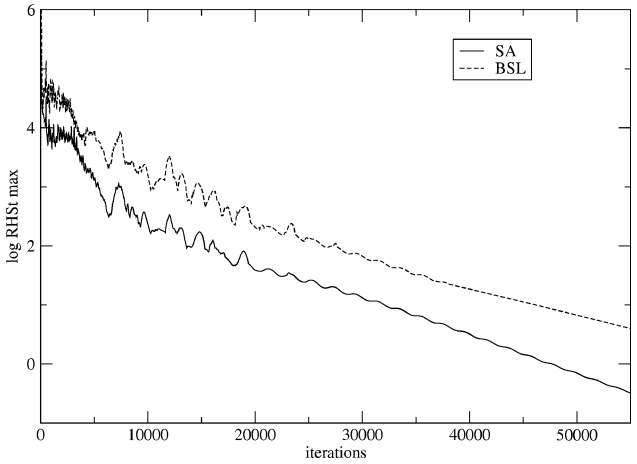

b) Turbulence equation

Fig. 5 Maximum residue histories for the numerical simulations over the VLS second-stage configuration at $M_\infty = 0.90$, $\alpha = 0$ deg, and $Re = 25 \times 10^6$.

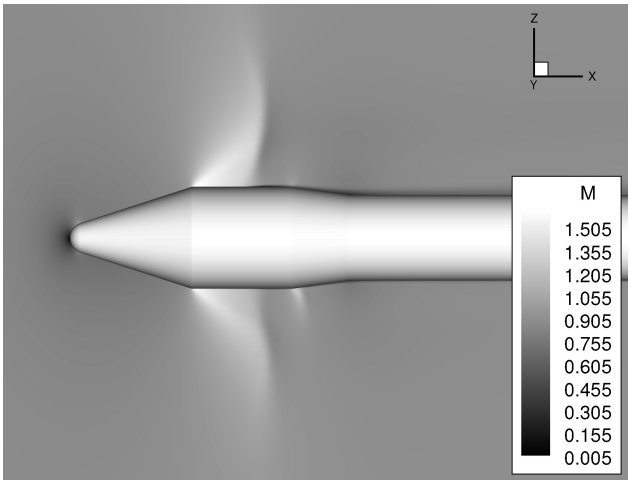

Fig. 6 Mach-number contours over the VLS second-stage configuration at $M_\infty = 0.90$, $\alpha = 4$ deg, and $Re = 25 \times 10^6$.

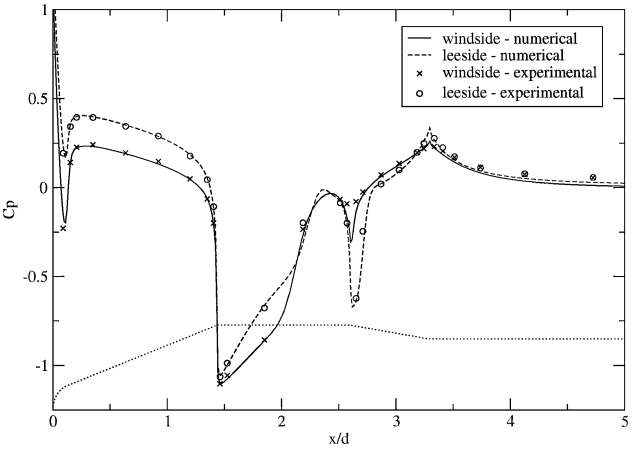

Fig. 7 Experimental and numerical *Cp* distributions over the VLS second-stage configuration at $M_\infty = 0.90$, $\alpha = 4$ deg, and $Re = 25 \times 10^6$.

along with the SST turbulence model successfully captures the interaction between the strong shock wave that builds up over the payload fairing region and the boundary layer, which results in the good agreement observed in Fig. 7. Velocity profiles and turbulent eddy viscosity contours at the region where the shock wave impinges on the boundary layer, in the vehicle payload fairing leeside, are presented in Fig. 8. One should observe the large velocity reduction produced by the shock wave in that region. The eddy viscosity, nevertheless, is computed in a suitable amount by the SST model to keep the flow attached through the shock wave, as seen in Fig. 8.

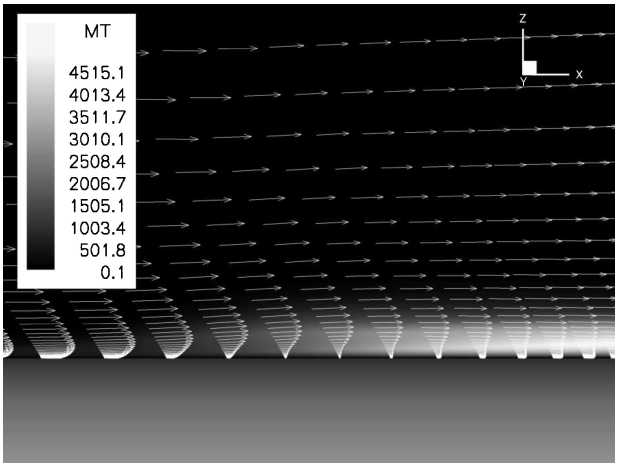

Fig. 8 Eddy viscosity contours and velocity profiles over the VLS payload fairing region, at $M_\infty = 0.90$ and $\alpha = 4$ deg ($Re = 25 \times 10^6$).

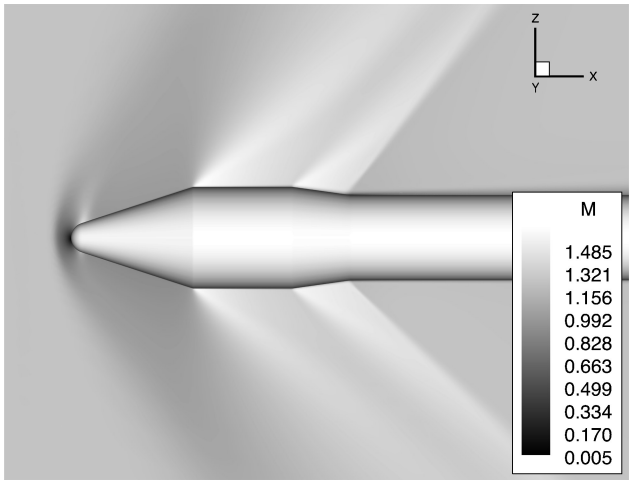

a) SA

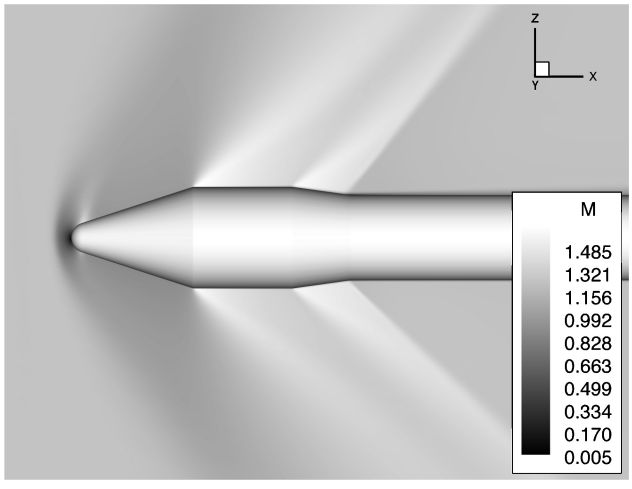

b) SST

Fig. 9 Mach-number contours over the VLS at $M_\infty = 1.25$ and $\alpha = 4$ deg ($Re = 22.4 \times 10^6$).

Supersonic Flight Condition

Turbulent flows with $M_\infty = 1.25$ and $\alpha = 4$ deg about the VLS second-stage flight configuration are considered. The Reynolds number associated with this flow is $Re = 22.4 \times 10^6$. This test case is intended to address the behavior of the SA and SST turbulence models in adverse pressure gradient regions. Mach-number contours obtained with the simulations with the turbulence models can be found in Fig. 9. All turbulence models capture well the position of the detached shock wave near the vehicle nose, as well as the expansion waves in the expansion corners of the geometry. An unfavorable pressure gradient, together with a shock wave, is found in the compression corner in the boattail-cylinder junction. This is a complicated region for the simulation because shock-wave boundary-layer interference surely occurs, dictating the local flow configuration. In this region, different behavior can be observed between the considered turbulence models, as shown in Fig. 10. In this figure, dimensionless eddy viscosity contours and velocity profiles are plotted. One can observe in Fig. 10 that the SST model computes lower values of eddy viscosity upstream from the compression corner, which yields lower velocities in this region than obtained with the SA model.

A quantitative analysis is also presented in Fig. 11. In this figure, Cp distributions over the VLS wall at the pitching plane are

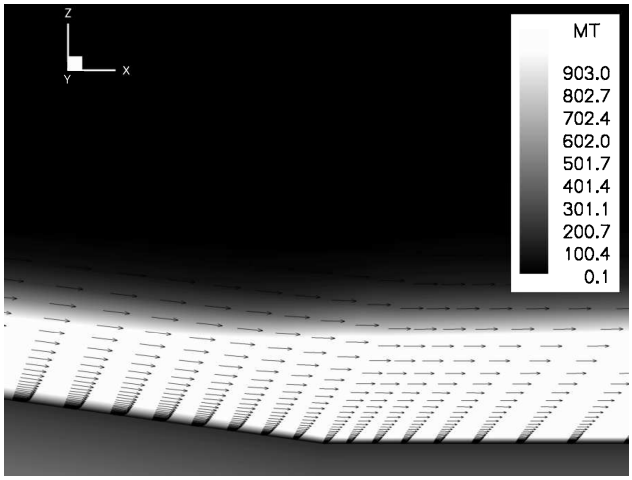

a) SA

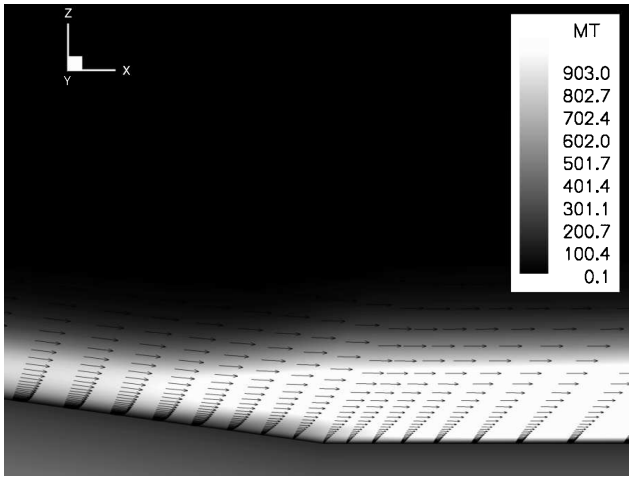

b) SST

Fig. 10 Eddy viscosity contours and velocity profiles over the VLS boattail-cylinder junction region, at $M_\infty = 1.25$ and $\alpha = 4$ deg ($Re = 22.4 \times 10^6$).

compared to available experimental data. As one can see in this figure, all turbulence models have similar and very good behavior in predicting the correct trends in the Cp distribution when compared to the experimental data, except in the compression corner at the vehicle leeside. A close view of this region is presented in Fig. 12. Both models have slightly different behavior, which is intimately associated with the differences observed in the eddy viscosity computation. The higher viscosity field computed by the SA model results in much stronger turbulent boundary layers, which are stiffer to the local adverse pressure gradient. The SST, however, computes lower turbulence levels in this region, resulting in weaker boundary layers, that are more sensitive to the local adverse pressure gradient. Nevertheless, the comparison with the experimental results shows, as seen in Fig. 12, that this behavior of the SST model is insufficient to correctly predict the experimentally observed slower recompression.

In Fig. 13, one can observe the y^+ distribution along the vehicle wall at the leeside and windside. One can observe in this figure that,

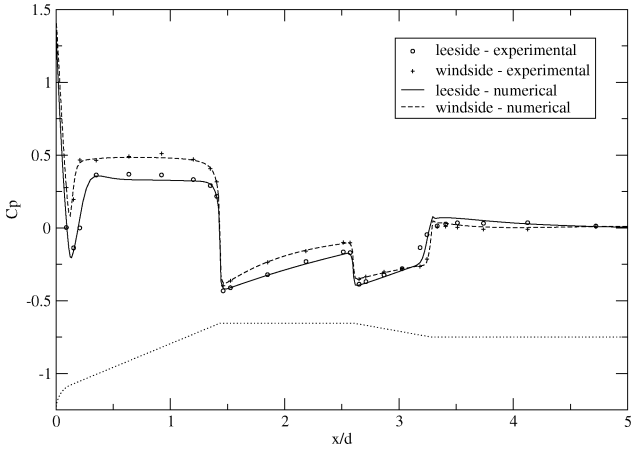

a) SA

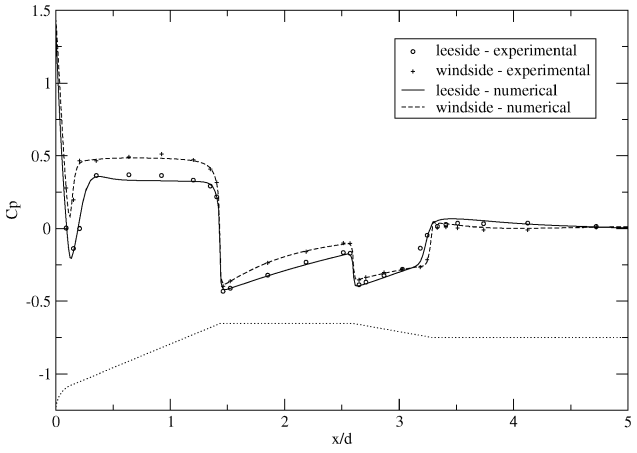

b) SST

Fig. 11 Wall *Cp* distributions over the VLS at $M_\infty = 1.25$ and $\alpha = 4$ deg ($Re = 22.4 \times 10^6$).

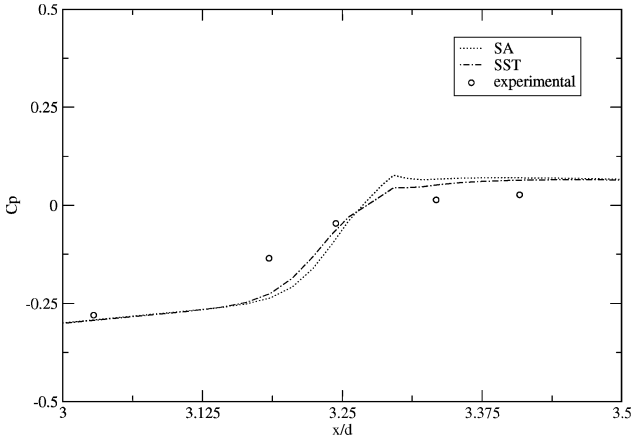

Fig. 12 Comparison of *Cp* distributions obtained with the SA and SST models at the boattail-cylinder junction for the VLS at $M_\infty = 1.25$ and $\alpha = 4$ deg ($Re = 22.4 \times 10^6$).

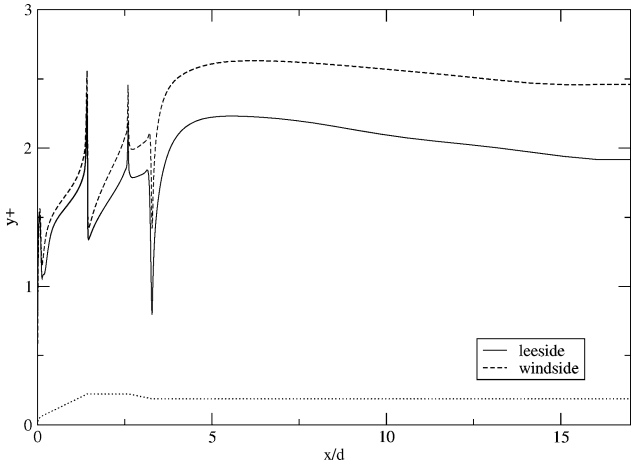

a) SA

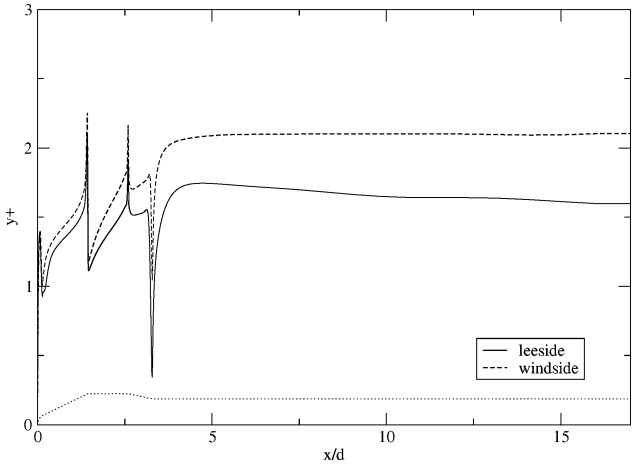

b) SST

Fig. 13 Distribution of y^+ along the VLS at $M_\infty = 1.25$ and $\alpha = 4$ deg ($Re = 22.4 \times 10^6$).

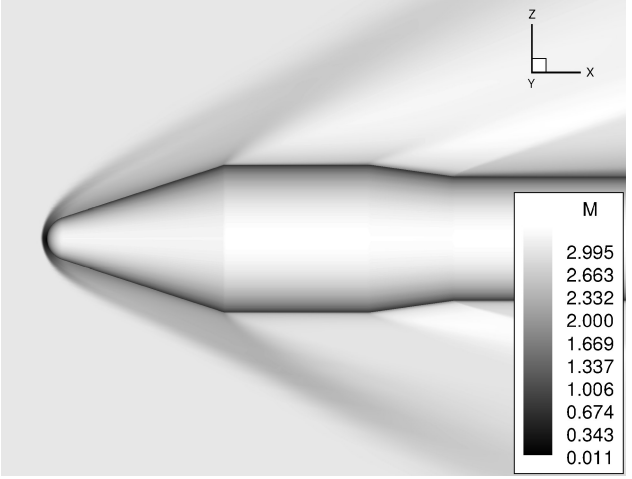

Fig. 14 Mach-number contours over the VLS second-stage configuration at $M_\infty = 3.00$, $\alpha = 4$ deg, and $Re = 29 \times 10^6$.

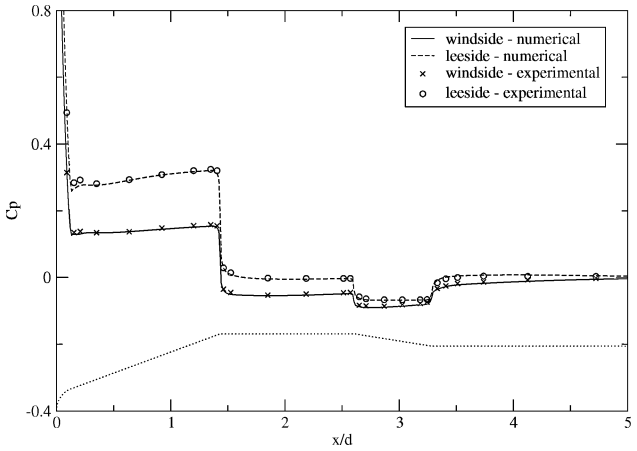

Fig. 15 Experimental and numerical *Cp* distributions over the VLS second-stage configuration at $M_\infty = 3.00$, $\alpha = 4$ deg, and $Re = 29 \times 10^6$.

despite the slight differences among each turbulence model, both kept this quantity around approximately two for both leeside and windside planes. This is enough for a correct behavior of the chosen turbulence models.

A higher Mach-number condition, namely, $M_\infty = 3.00$, and angle of attack $\alpha = 4$ deg, is also considered. The Reynolds number for this flight condition is $Re = 29 \times 10^6$, and the SST turbulence model has been used in the simulation. Mach-number contours for this flow case can be found in Fig. 14. Numerical Cp distributions for the vehicle leeside and windside are compared to the respective experimental results in Fig. 15. Very good approximation between numerical and experimental results can be observed for this more demanding flight condition.

Conclusions

This work presents the assessment of the newly implemented turbulent three-dimensional flow solver capability at IAE. This numerical tool is aimed at solving three-dimensional flows over complex aerospace configurations at angle of attack to determine important aerodynamic loads required at the design stage. Previous results showed the need for incorporating robust turbulent closures to the computational code in order to correctly address the transonic and supersonic flows about such complex geometries. A computational code that solves the compressible Reynolds-averaged Navier–Stokes equations for general, body-conforming, curvilinear coordinates is used. The Spalart–Allmaras single-equation model and the Menter BSL/SST two-equation turbulence closure have been implemented into the code in order to include the turbulent influence into the governing equations. The numerical code is used to simulate the subsonic flow about a flat plate and transonic and supersonic flows about the VLS central body configuration.

The verification analyses involve the comparison of zero-pressure-gradient flat-plate turbulent boundary layers with the theoretical log-layer law. Very good agreement between the numerical and the theoretical results is obtained. The numerical results for the simulation of the VLS are, then, compared to experimental data in order to further assess the quality of the computational tool. In general, good results are obtained, which show the capability of this code to adequately address the flows of interest at IAE. Nevertheless, the results have shown that the prediction of recompression regions could be further improved, indicating the need for more advanced turbulence closures to correctly capture such phenomena.

An analysis of the computational resources necessary to simulate the turbulent flows shows that one turbulent iteration costs about twice that of an inviscid step for a given problem. Furthermore, the condition of satisfying $y^+ = 1$ for the first point away from the wall yields more stretched and refined computational meshes. Convergence is accelerated with variable time step, implicit residual smoothing, and multigrid techniques. The use of multigrid and implicit residual smoothing techniques can result in convergence rates that are about twice as fast as the ones obtained with the variable time-step option alone. The results presented here are a good indication of the level of accuracy that can be attained with the computational tool.

Acknowledgments

The present work was partially supported by Conselho Nacional de Desenvolvimento Científico e Tecnológico, CNPq, under Integrated Project Research Grants 522413/96-0 and 501200/2003-7. The authors are also indebted to Fundação de Amparo à Pesquisa do Estado de São Paulo, FAPESP, which provided the first author with a graduate scholarship under Process 00/13652-6. The authors also acknowledge the Centro Nacional de Supercomputação, at Universidade Federal do Rio Grande do Sul, for providing the necessary computational resources to address the turbulent simulations presented in this work.

References

[1]Zdravistch, F., and Azevedo, J. L. F., "Numerical Simulation of High Speed Flows over Complex Satellite Launchers," *Proceedings of the 3rd Brazilian Thermal Sciences Meeting—ENCIT 90*, Vol. 1, edited by C. R. Maliska, C. Melo, and A. T. Prata, Itapema, Brazil, 1990, pp. 233–238.

[2]Azevedo, J. L. F., Zdravistch, F., and Silva, A. F. C., "Implementation and Validation of Euler Solvers for Launch Vehicle Flows," *Proceedings of the Fourth International Symposium on Computational Fluid Dynamics*, Vol. 1, Univ. of California, Davis, CA, 1991, pp. 42–47.

[3]Azevedo, J. L. F., Strauss, D., and Ferrari, M. A. S., "Viscous Multiblock Simulations of Axisymmetric Launch Vehicle Flows," *Journal of Spacecraft and Rockets*, Vol. 36, No. 4, 1999, pp. 489–498.

[4]Azevedo, J. L. F., Moraes, P., Jr., Maliska, C. R., Marchi, C. H., and Silva, A. F. C., "Code Validation for High-Speed Flow Simulation over Satellite Launch Vehicle," *Journal of Spacecraft and Rockets*, Vol. 33, No. 1, 1996, pp. 15–21.

[5]Azevedo, J. L. F., and Buonomo, C. A., "Axisymmetric Turbulent Simulations of Launch Vehicle Forebody Flows," AIAA Paper 99-3528, June–July 1999.

[6]Bigarelli, E. D. V., Mello, O. A. F., and Azevedo, J. L. F., "Three Dimensional Flow Simulations for Typical Launch Vehicles at Angle of Attack," *Proceedings of the 15th Brazilian Congress of Mechanical Engineering—COBEM 99* [CD-ROM], edited by J. R. F. Aruda, Brazilian Society of Mechanical Sciences and Engineering, Rio de Janeiro, Brazil, 1999.

[7]Bigarelli, E. D. V., Cruz, L. R. S., Azevedo, J. L. F., and Mello, O. A. F., "Normal Force Calculations for a Typical Launch Vehicle Configuration," *Proceedings of the XXII Iberian Latin American Congress on Computational Methods in Engineering—XXII CILAMCE* [CD-ROM], Universidade de Campinas, Campinas, Brazil, 2001.

[8]Moraes, P., Jr., and Augusto Neto, A., "Aerodynamic Experimental Investigation of the Brazilian Satellite Launch Vehicle (VLS)," *Proceedings of the 3rd Brazilian Thermal Sciences Meeting—ENCIT 90*, Vol. 1, edited by C. R. Maliska, C. Melo, and A. T. Prata, Itapema, Brazil, 1990, pp. 211–215.

[9]Pulliam, T. H., and Steger, J. L., "Implicit Finite-Difference Simulations of Three-Dimensional Compressible Flow," *AIAA Journal*, Vol. 18, No. 2, 1980, pp. 159–167.

[10]Turkel, E., and Vatsa, V. N., "Effect of Artifical Viscosity on Three-Dimensional Flow Solutions," *AIAA Journal*, Vol. 32, No. 1, 1994, pp. 39–45.

[11]Jameson, A., Schmidt, W., and Turkel, E., "Numerical Solution of the Euler Equations by Finite Volume Methods Using Runge–Kutta Time-Stepping Schemes," AIAA Paper 81-1259, June 1981.

[12]Jameson, A., and Mavriplis, D., "Finite Volume Solution of the Two-Dimensional Euler Equations on a Regular Triangular Mesh," *AIAA Journal*, Vol. 24, No. 4, 1986, pp. 611–618.

[13]Swanson, H., and Turkel, E., "Multistage Schemes with Multigrid for Euler and Navier–Stokes Equations. Components and Analysis," NASA TP 3631, Aug. 1997.

[14]Fletcher, C. A. J., *Computational Techniques for Fluid Dynamics 1. Fundamental and General Techniques*, Springer-Verlag, Berlin, 1988, Chap. 6, pp. 203–209.

[15]Bigarella, E. D. V., "Three-Dimensional Turbulent Flow Simulations over Aerospace Configurations," M.S. Thesis, Inst. Technológico de Aeronáutica, São José dos Campos, Brazil, Dec. 2002.

[16]Beam, R. M., and Warming, R. F., "An Implicit Factored Scheme for the Compressible Navier–Stokes Equations," *AIAA Journal*, Vol. 16, No. 4, 1978, pp. 393–402.

[17]Steger, J. L., and Warming, R. F., "Flux Vector Splitting of the Inviscid Gasdynamic Equations with Application to Finite-Difference Methods," *Journal of Computational Physics*, Vol. 4, No. 2, 1981, pp. 263–293.

[18]Spalart, P. R., and Allmaras, S. R., "A One-Equation Turbulence Model for Aerodynamic Flow," *La Recherche Aeropastiale*, Vol. 1, No. 1, 1994, pp. 5–21.

[19]Menter, F. R., "Zonal Two Equation $k-\omega$ Turbulence Models for Aerodynamic Flows," AIAA Paper 93-2906, July 1993.

[20]Wilcox, D. C., "Comparison of Two-Equation Turbulence Models for Boundary Layers with Pressure Gradient," *AIAA Journal*, Vol. 31, No. 8, 1993, pp. 1414–1421.

[21]Jones, W. P., and Launder, B. E., "The Prediction of Laminarization with a Two-Equation Model of Turbulence," *International Journal of Heat and Mass Transfer*, Vol. 15, No. 2, 1972, pp. 301–314.

[22]Menter, F. R., "Two-Equation Eddy-Viscosity Turbulence Models for Engineering Applications," *AIAA Journal*, Vol. 32, No. 8, 1994, pp. 1598–1605.

[23]Azevedo, J. L. F., Fico, N. G. C. R., Jr., and Ortega, M. A., "Two-Dimensional and Axisymmetric Nozzle Flow Computations Using the Euler Equations," *Journal of the Brazilian Society of Mechanical Sciences*, Vol. 17, No. 2, 1995, pp. 147–170.

[24]Long, L. N., Khan, M., and Sharp, H. T., "A Massively Parallel Three-Dimensional Euler/Navier–Stokes Method," *AIAA Journal*, Vol. 29, No. 5, 1991, pp. 657–666.

[25]Ying, S. X., "Three-Dimensional Implicit Approximately Factored Schemes for the Equations of Gasdynamics," Dept. of Aeronautics and Astronautics, Stanford Univ., SUDAAR 557, Stanford, CA, June 1986.

[26]Roache, P. J., *Verification and Validation in Computational Science and Engineering*, Hermosa, Albuquerque, NM, 1998.

[27]Strauss, D., "An Unstructured Grid Approach to the Solution of Axisymmetric Launch Vehicle Flows," M.S. Thesis, Inst. Technológico de Aeronáutica, São José dos Campos, Brazil, Nov. 2001.

[28]Basso, E., Antunes, A. P., and Azevedo, J. L. F., "Three Dimensional Flow Simulations over a Complete Satellite Launcher with a Cluster Configuration," AIAA Paper 2000-4514, Aug. 2000.

[29]Basso, E., Antunes, A. P., and Azevedo, J. L. F., "Chimera Simulations of Supersonic Flows over a Complex Satellite Launcher Configuration," *Journal of Spacecraft and Rockets*, Vol. 40, No. 3, 2003, pp. 345–355.

R. Cummings
Associate Editor